JACS
JOURNAL OF THE AMERICAN CHEMICAL SOCIETY
pubs.acs.org/JACS
Article

Variable Peripheral Ligand Donation Tunes Electronic Structure and NIR II Emission in Tetrathiafulvalene Tetrathiolate Diradicaloids

Lauren E. McNamara, Jan-Niklas Boyn, Sophie W. Anferov, Alexander S. Filatov, Miles W. Maloney, David A. Mazziotti, Richard D. Schaller, and John S. Anderson*

Cite This: J. Am. Chem. Soc. 2024, 146, 17285−17295

ABSTRACT: Near-infrared (NIR) lumiphores are promising candidates for numerous imaging, communication, and sensing applications, but they typically require large, conjugated scaffolds to achieve emission in this low-energy region. Due to the extended conjugation and synthetic complexity required, it is extremely difficult to tune the photophysical properties of these systems for desired applications. Here, we report facile tuning of deep NIR-emitting diradicaloid complexes through simple modification of peripheral ligands. These new lumiphores are rare examples of air-, acid-, and water-stable emissive diradicaloids. We apply a simple Hammett parameter-based strategy to tune the electron donation of the capping ligand across a series of commercially available triarylphosphines. This minor peripheral modification significantly alters the electronic structure, and consequently, the electrochemical, photophysical, and magnetic properties of the tetrathiafulvalene tetrathiolate (TTFtt)-based lumiphores. The resultant ∼100 nm absorption and emission range spans common laser lines and the desirable telecom region (ca. 1260−1550 nm). Furthermore, these lumiphores are sensitive to local dielectrics, distinguishing them as promising candidates for ratiometric imaging and/or barcoding in the deep NIR region.

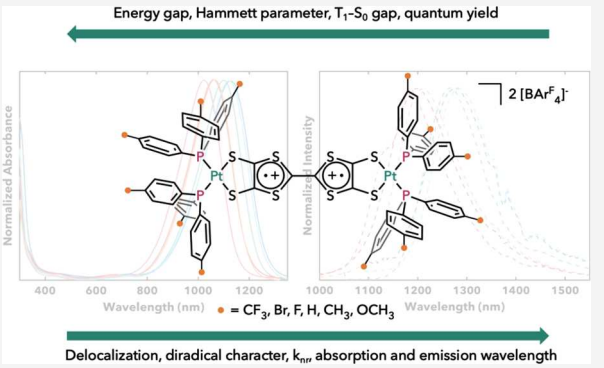

INTRODUCTION

Near-infrared (NIR, 700−1700 nm) emitting molecules are promising for several imaging and sensing applications;[1−9] however, current Food and Drug Administration (FDA)-approved dyes emit on the blue edge of this region where image quality suffers from high scattering and autofluorescence.[1,2] Ideally, emission centered in the NIR II (1000−1700 nm) region would prevent these deleterious processes and thus improve image quality.[1] Leading NIR II-emitting lumiphores rely on complex scaffolds with large, conjugated motifs to shift absorption and emission energies into this low-energy region;[1,10,11] however, these complex scaffolds prevent facile synthetic tuning of photophysical properties. Scaffolds with tunable NIR absorption/emission would be valuable as they would also allow for targeted and multicolor imaging.[12,13] Furthermore, multicolor imaging can additionally be enhanced and leveraged with dyes that are responsive to various environments; this approach can give additional environmental information as a result of emission or absorption shifts.[12−16] In addition to NIR II bioimaging, complexes that emit in the low attenuation telecom bands (∼1260−1550 nm) are of special interest for communication-related applications.[17,18] In particular, open-shell complexes that emit in this region would be ideal candidates for sensing and transmitting quantum information.

Our lab has recently reported a compact, modular scaffold that emits deep into the NIR II, while maintaining high photoluminescence quantum yields (PLQYs) for the region.[19] While our previously reported analogues displayed some modularity in electronic structure and photophysical properties, we wanted to test whether systematic perturbations would enable rational tuning of these properties over a wider range and thus allow for more targeted applications.[19,20] Using triarylphosphines as a set of tunable capping ligands, we introduced various electron-donating and -withdrawing groups to the para position of the aryl rings. This approach enabled the synthesis of four new Pt-capped tetrathiafulvalene tetrathiolate (TTFtt) dicationic complexes. We then compared the electronic structures and photophysical properties of these complexes with two previously reported examples for a total comparison across six analogues.[19,20]

Surprisingly, we found that these facile and relatively minor perturbations have large impacts on electronic structure:

Received: March 21, 2024
Revised: May 3, 2024
Accepted: June 3, 2024
Published: June 14, 2024

https://doi.org/10.1021/jacs.4c04032
J. Am. Chem. Soc. 2024, 146, 17285−17295

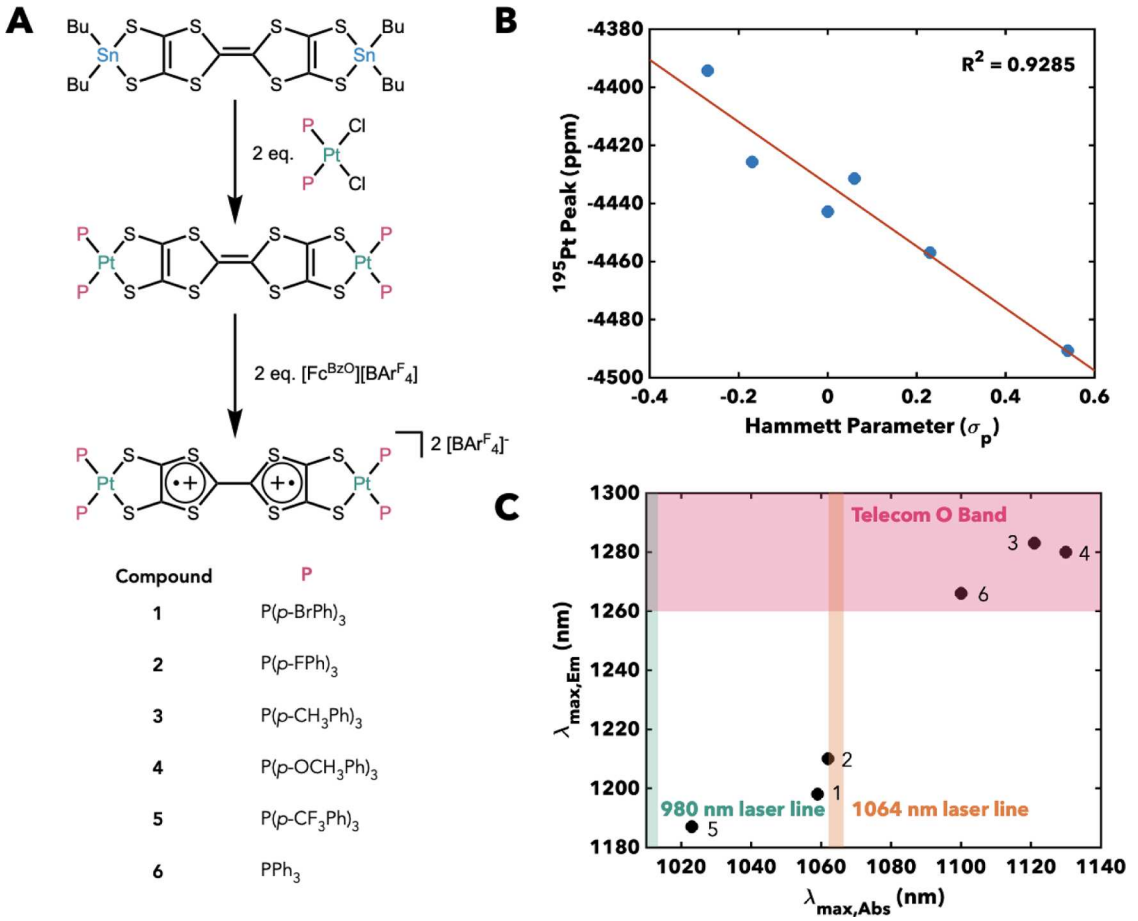

Compound	P
1	$P(p\text{-}BrPh)_3$
2	$P(p\text{-}FPh)_3$
3	$P(p\text{-}CH_3Ph)_3$
4	$P(p\text{-}OCH_3Ph)_3$
5	$P(p\text{-}CF_3Ph)_3$
6	PPh_3

Figure 1. (A) Synthetic scheme for **1**−**6**. (B) Relationship between Hammett parameter and observed ^{195}Pt signal in CD_2Cl_2. (C) Plot of absorption and emission across Hammett series, overlaid with common laser lines and telecom region.

absorption and emission maxima shift by hundreds of nanometers, electrochemical potentials shift by hundreds of millivolts, the ground state T_1−S_0 gap changes by several kcal/mol, and the overall diradical character increases by 28%. Furthermore, we observe that these properties are responsive to the local environment of the lumiphore; the absorption and emission can be shifted significantly as a function of solvent dielectric. Lastly, these air-, acid-, and water-stable compounds are soluble in aqueous solutions, distinguishing them as promising biological sensors.

The desirable tunability and resultant photophysical and magnetic properties of this system are directly enabled by the compact TTFtt core at the center of each molecule. This NIR II emission is realized on such a small core due to heavy heteroatom substitution, which compresses the π system and bathochromically shifts emission.[21] Furthermore, the compact scaffold size minimizes deleterious vibrational modes that are believed to enhance nonradiative decay in this region.[20] Ultimately, the capping of this small scaffold with Pt centers maintains this bright, organic-based NIR II emission, while allowing for tunability on the open capping ligand sites.

RESULTS AND DISCUSSION

Synthesis and Characterization of Pt TTFtt Analogues. We designed our study based off current commercially available triarylphosphines with variable substituents in the para position. We already had used two such analogues to synthesize new TTFtt complexes for previous studies (CF_3 and H with Hammett parameters, σ_p, 0.54 and 0, respectively).[19,20,22] We expanded the series with the addition of four new analogues for a total range of Hammett parameters from −0.27 to 0.54.[22]

We synthesized the Pt phosphine dichloride precursors based on modified literature procedures (see the Supporting Information (SI)), using commercially available, *p*-substituted triarylphosphines.[23−26] The Pt precursors were then reacted with $(SnBu_2)_2$TTFtt and subsequently oxidized with two equivalents of $[Fc^{BzO}][BAr_4^F]$, according to previously established procedures, to give the dicationic complexes **1**−**4** (see Figure 1).[27] These complexes, along with previously reported analogues **5** and **6**, form a series of *p*-substituted triphenylphosphine-capped dications.[19,20] These complexes were characterized by a suite of techniques, including multinuclear NMR spectroscopy and single-crystal X-ray diffraction (SXRD). SXRD-quality crystals were grown by layering hexanes or petroleum ether over the desired complex dissolved in dichloromethane (DCM), forming a slow diffusion gradient. The SXRD structures reveal minor variations in central C3−C4 distances for complexes **1**−**3**. In contrast, complex **4** has a noticeably shorter distance of 1.34 Å; however, this shortening may be convoluted due to packing effects as **4** crystallizes differently than the other analogues and forms π-stacks in the solid state. Previous studies have correlated shorter C3−C4 distances to increased diradical character, thus suggesting that these peripheral ligand substitutions may significantly tune electronic structure.[28]

https://doi.org/10.1021/jacs.4c04032
J. Am. Chem. Soc. 2024, 146, 17285−17295

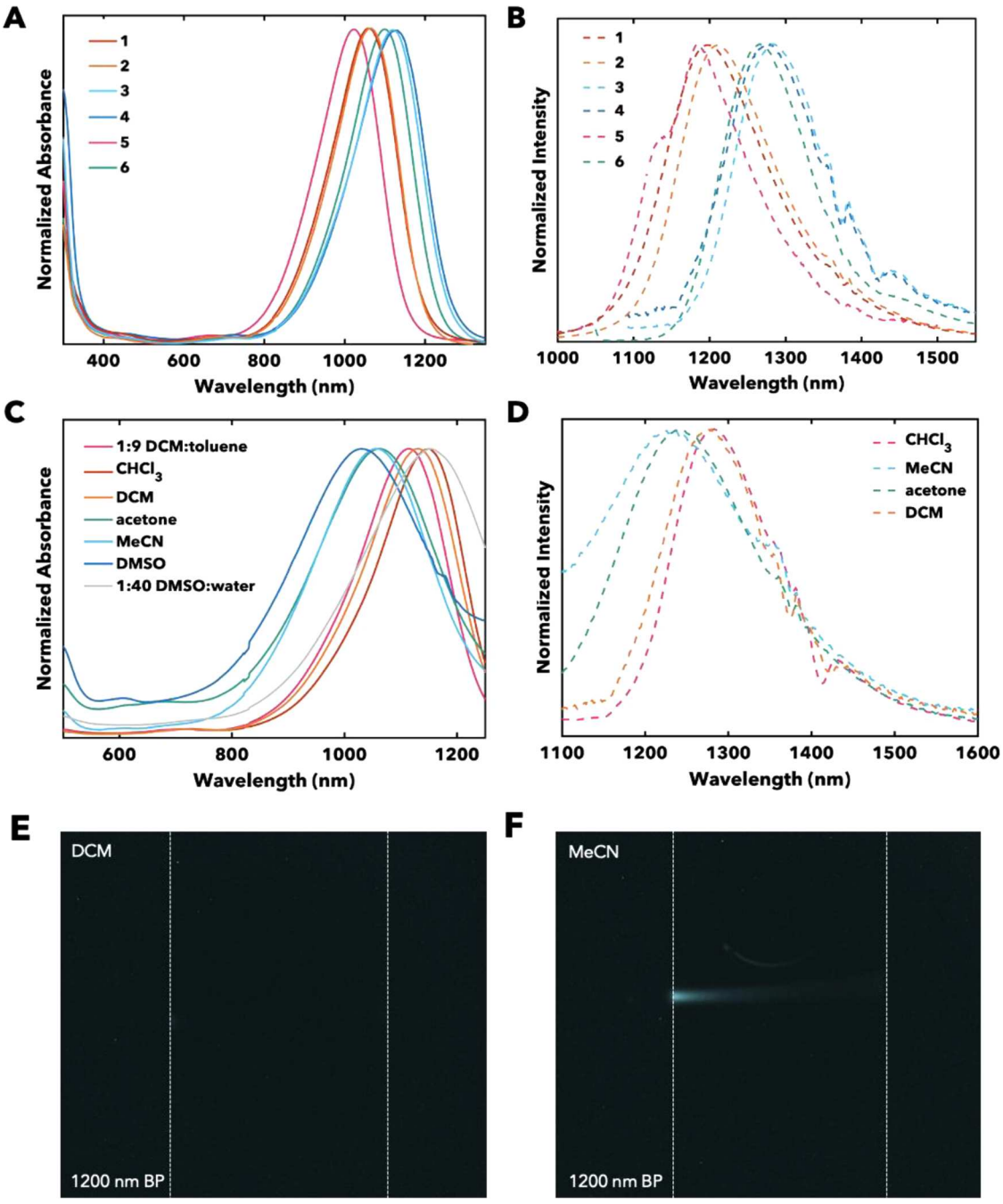

Figure 2. (A) UV−vis−NIR spectra across all six analogues in DCM at 296 K. (B) Photoluminescence spectra across all six analogues in DCM at 296 K. (C) UV−vis−NIR of **4** across various solvents. (D) Photoluminescence of **4** across various solvents. (E) Colorized NIR image of **4** in DCM (100 μM) using a 1200 nm bandpass filter, 808 nm excitation, and 800 ms exposure. (F) Colorized NIR image of **4** in MeCN (100 μM) using a 1200 nm bandpass filter, 808 nm excitation, and 800 ms exposure.

NMR analyses confirm that these peripheral ligand modifications modulate the electronics of the Pt phosphine moiety; ^{195}Pt NMR signals respond linearly with Hammett parameter, demonstrating electronic structure modification by the capping fragment (see Figure 1B). Furthermore, J_{Pt-P} and ^{31}P shifts also trend linearly with Hammett parameter, indicating that the general donation strength of the phosphine is indeed being modified by the para substituent (see Figures S94 and S95).

Photophysical Characterization and Tuning. Complexes **1**−**6** display intense NIR absorption peaks in DCM, with extinction coefficients (ε) ranging from ca. 80,000 to 150,000 M^{-1} cm^{-1}. The NIR peak maxima span 1023−1130 nm, a range >100 nm/900 cm^{-1} (Figure 2A). These absorption maxima shift linearly with the Hammett parameter of the para group, σ_p, validating this parameter as a simple predictive tool to design systems absorbing at specific wavelengths and further supporting how peripheral ligand changes can tune the electronic structure of the TTFtt moiety.[22] Additionally, all six analogues emit brightly in DCM, with emission maxima spanning ∼100 nm (∼630 cm^{-1}), from 1187 to 1283 nm (Figure 2B, shoulders near 1150, 1380, and 1420 nm arise from DCM absorptions). Unlike the absorption data, plotting these emission maxima against σ_p reveals that the

https://doi.org/10.1021/jacs.4c04032
J. Am. Chem. Soc. 2024, 146, 17285−17295

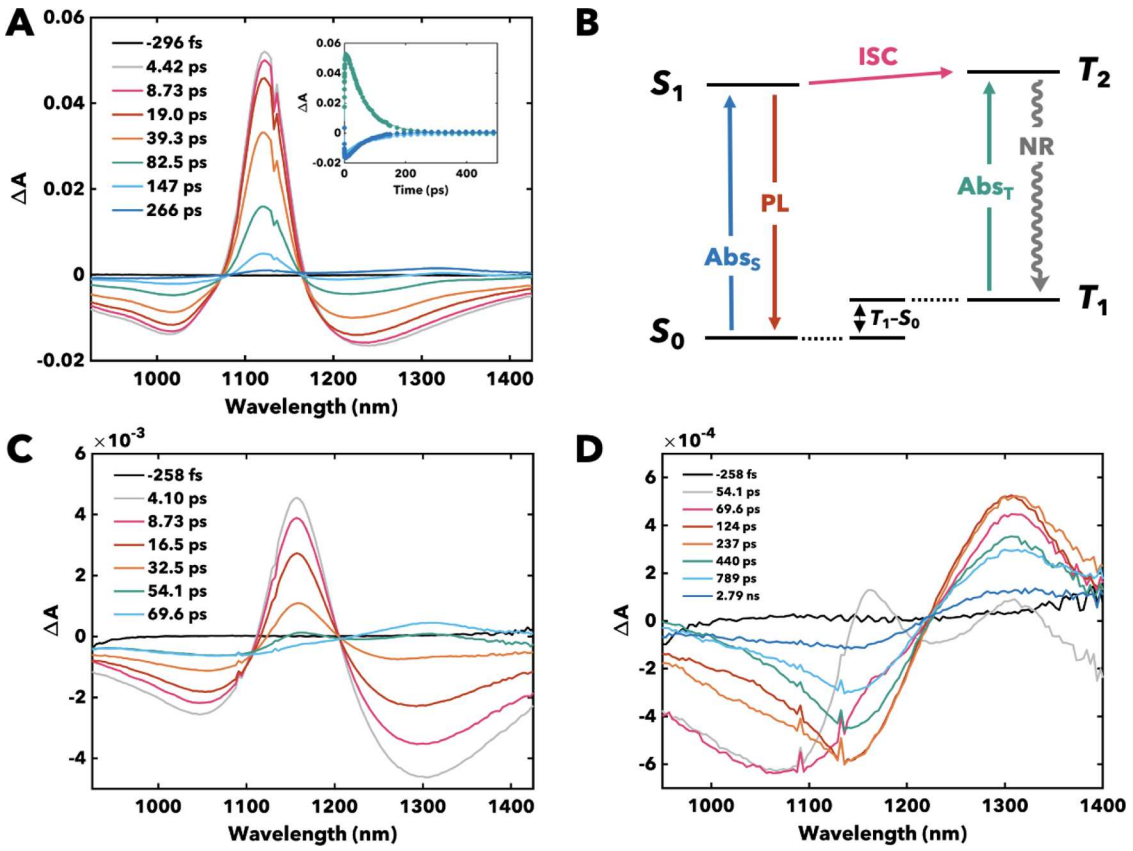

Figure 3. (A) Decay of TA spectra of **1** in DCM at 298 K. Inset: transient kinetics of the three key features of **1** in DCM at 298 K. (B) General Jablonski diagram for series of complexes **1**−**6**. (C) Decay of TA spectra of **4** in DCM at 298 K. (D) Decay of TA spectra of **4** in DCM at 298 K, taken at longer time points.

six analogues fall into two distinct bands, spaced roughly 300 cm^{-1} apart. A previous study suggested this spacing is consistent with TTFtt skeletal vibrations, so it is possible the separation into these two bands is a result of changing vibronic overlap.[20]

Calculations suggest that solvatochromic behavior should be observed for these complexes. Across all analogues, the ground state has a larger dipole moment than the excited state, consistent with an expected negative solvatochromic trend (see Table S9). Complex **4** is predicted to have a moderate solvatochromic shift and thus was chosen as an example for study across a wide range of dielectrics. Interestingly, the NIR absorption peaks of complex **4** can be further tuned via this method, increasing the available range to 950−1155 nm (~10,525−8650 cm^{-1}); emission is similarly expanded to ca. 1110−1283 nm (ca. 9010−7790 cm^{-1}, see Figure 2C,D, this range includes previously reported data for **5**).[19] Consistent with theory, these dyes display a strong negative solvatochromic trend, although we note that aqueous mixtures appear to deviate from this trend. We propose that this deviation is likely due to increased aggregation; however, aggregation does not completely prevent emission in aqueous mixtures, as emission was still detected by our NIR imaging setup in 1:1 water/MeCN and water/dimethyl sulfoxide (DMSO) solutions (see Figure S81).

This broad solvatochromic response is noteworthy and is the first time such a response has been reported centered in the deep NIR II region (>1200 nm). This behavior distinguishes these dyes as promising candidates for sensing small environmental shifts and offers an additional handle to optimize these systems for common laser lines (see Figures 1C and 2C,D). We utilized this solvatochromic behavior to demonstrate proof-of-concept ratiometric imaging using a 1200 nm bandpass filter and two different solvent dielectrics (see Figure 2E,F). Emission at 1200 nm from compound **4** is visible in a higher dielectric medium (MeCN), but nearly undetectable at lower dielectrics due to the bathochromically shifted emission peak in DCM (see Figure 2D). We believe this is a promising area of future investigation and application for these compounds.

The absorption and emission peak shifts across **1**−**6** are also ideal for thin film applications. NIR barcoding has been of interest for security and pharmaceutical applications, and such tunable compounds would be of particular interest due to the added complexity multiple NIR II wavelengths provide.[29−32] We tested this application by drop-casting polymer films of **1**−**6** onto a microscope slide and applying long-pass and bandpass filters. These compounds have weak visible absorptions, so the films are nearly colorless to the eye; however, upon 808 nm excitation, they brightly emit in the NIR II region. Furthermore, they retain their capping ligand-induced wavelength shifts as thin films, so bandpass filters can distinguish between individual compounds (see Figures S83−S85).

We further investigated the electronic underpinnings of these absorption and emission shifts across σ_p with transient absorption (TA) spectroscopy. The TA spectra of compounds **1**−**4** display a ground state bleach (GSB) between 1000 and 1100 nm, an excited state absorption (ESA) at ~1130 nm, and a stimulated emission (SE) feature between 1200 and 1300 nm

https://doi.org/10.1021/jacs.4c04032
J. Am. Chem. Soc. 2024, 146, 17285−17295

Table 1. Experimental and Theoretical Photophysical Parameters[a]

	1	2	3	4
$\lambda_{Abs,exp}$ (nm)	1059	1062	1121	1130
$\lambda_{Em,exp}$ (nm)	1198	1210	1283	1280
$\lambda_{Abs,th,S}$ (nm)	1038	1090.2	1071.5	1141
$\lambda_{Em,th,S}$ (nm)	1140.5	1146	1178.6	1190
$\lambda_{Abs,th,T}$ (nm)	1156.4	1147.5	1140.7	1142.9
$\tau_{TA,S}$ (ps)	64.5 ± 5.2	54.8 ± 5.1	27.4 ± 3.9	22.0 ± 4.4
ε (M^{-1} cm^{-1})	80,868	102,884	84,524	94,808
k_{nr} (s^{-1})	1.55×10^{10}	1.82×10^{10}	3.65×10^{10}	4.55×10^{10}
k_r (s^{-1})	2.65×10^{7}	2.57×10^{7}	2.04×10^{7}	1.86×10^{7}
PLQY (%)	0.171	0.141	0.056	0.041

[a]Lifetimes, extinction coefficients, and PLQYs acquired in DCM at 298 K. Nonradiative and radiative rates are calculated using TA lifetimes. See the SI and Methods for details. "exp" and "th" stand for experimentally and theoretically obtained values, respectively. "S" and "T" indicate singlet and triplet transitions, respectively.

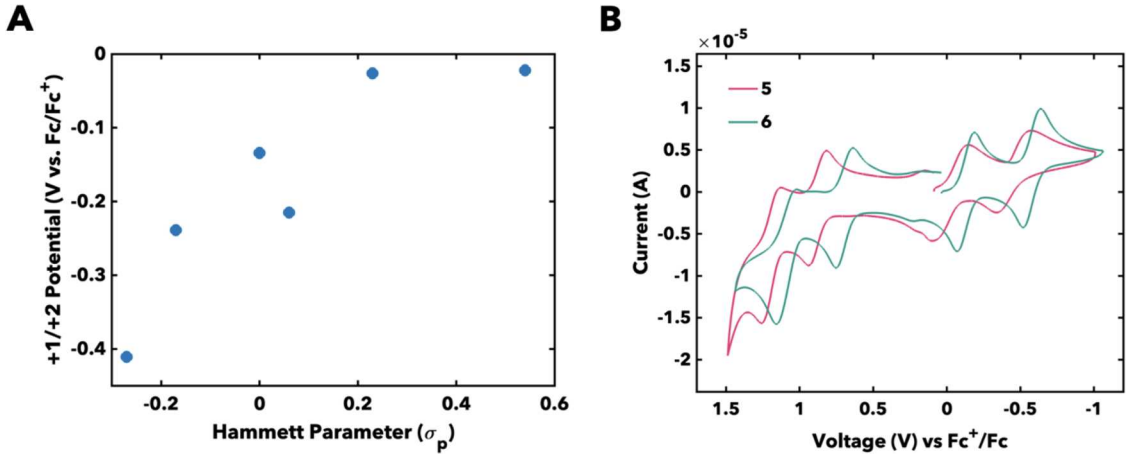

Figure 4. (A) Relationship between Hammett parameter and +1/+2 TTFtt redox couple potential in DCM. (B) Overlayed cyclic voltammograms of **5** and **6** in DCM (0.1 M [TBA][PF_6], scan rate 0.1 V/s).

(see Figure 3). These features have been previously assigned as the population of the S_1 state.[19]

TA and time-correlated single photon counting (TCSPC) measurements reveal singlet (S_1, see Figure 3A, inset) lifetimes that trend linearly with Hammett parameter (see Table 1 and Figure S99). Furthermore, the GSB appears to shift after population of T_2 (previously assigned to the spectra that emerges at long time points after decay of S_1), potentially a result of the close-lying singlet and triplet absorptions and the relatively slower decay of T_2 compared to S_1.

Photoluminescence quantum yield (PLQY) values range from 0.43 to 0.04% and trend exponentially with Hammett parameter (see Figures S96 and S97), as do the radiative (k_r) and nonradiative rates (k_{nr}, see Figures S100 and S101). The observed order of magnitude PLQY decrease (and k_{nr} increase) is consistent with the empirical observation known as the energy gap law, which predicts exponential increases in the nonradiative decay rate as the transition energy decreases (see Figure S98).[33−35] Using these PLQY values, we calculated "brightness", which is defined as the product of PLQY and extinction coefficient.[36] For this series of six dyes, the brightness values in DCM range from ∼4000 to 60,000 M^{-1} cm^{-1}, among the highest in the NIR II region.[36] Finally, we investigated photostability under 808 nm irradiation (see Figures S77 and S78). Over the course of 9 h, no decrease in absorption or emission was observed, distinguishing these compounds as remarkably photostable NIR II dyes.

Lastly, because NIR II gastrointestinal imaging is of interest, we tested the stability and brightness of this class of compounds in acid.[37,38] Interestingly, these compounds dissolve and retain stability and brightness in glacial acetic acid (see Figures S75, S76, and S82). Acid stability is rare among NIR molecular lumiphores, so this will be a promising area of future investigation for these compounds.[37]

Redox Tuning. The electrochemical properties of these analogues were investigated to determine if these minor synthetic perturbations had any effect on the redox potentials of the +1/+2 TTFtt couple. This couple is of particular importance since it is correlated with lumiphore stability, especially under reducing biological conditions. Reduction to the monocation is problematic due to induced redox stress in a biological system, as well as competing low-energy monocation absorptions (∼1250 nm) which overlap with the dication emission.[27]

Interestingly, the +1/+2 redox potential has a nonlinear, roughly exponential relationship with Hammett parameter (see Figure 4). The potentials range over nearly 400 mV, from −0.022 to −0.411 V vs Fc/Fc^+, demonstrating significant tunability. The exponential dependency at negative Hammett values suggests it is likely that even a slightly more donating group than OMe would result in significantly more reductively stable lumiphores.

Theoretical Description of Electronic Structure. The electronic structure changes apparent in the spectroscopic data

https://doi.org/10.1021/jacs.4c04032
J. Am. Chem. Soc. 2024, 146, 17285−17295

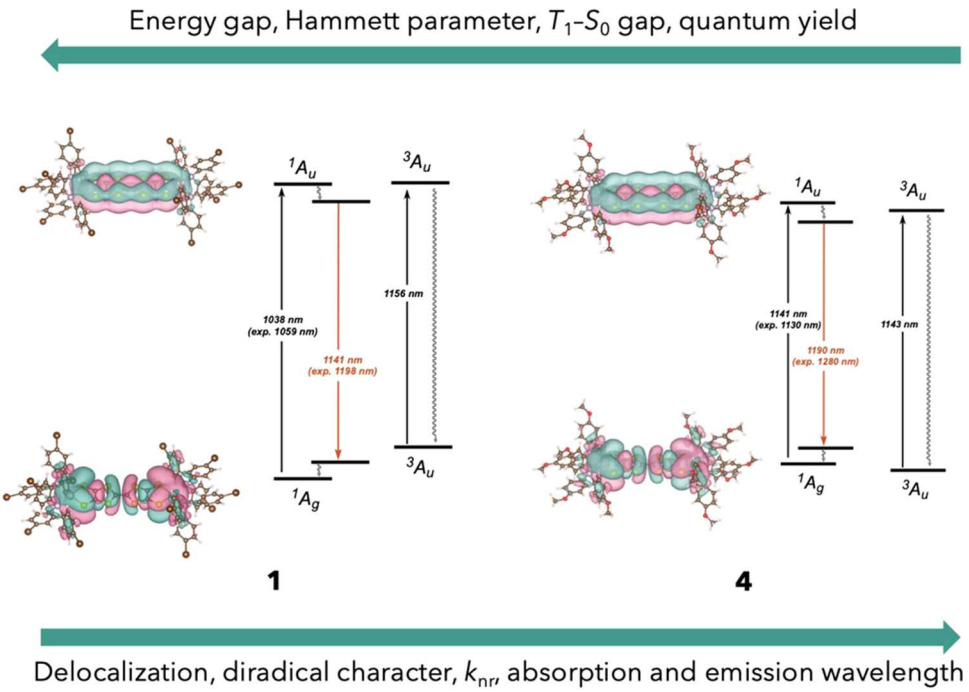

Figure 5. Computed Jablonski diagrams and NTOs of compounds **1** (left) and **4** (right), showing the decrease in transition energy gap with Hammett parameter of the para-substituted group on the peripheral capping ligands. ^1A_g and ^1A_u correspond to S_0 and S_1, respectively. The upper ^3A_u and lower ^3A_u correspond to T_2 and T_1, respectively.

are supported by time-dependent density functional theory (TD-DFT) and complete active-space self-consistent field (CASSCF) calculations both carried out as implemented in ORCA 5.0.3.[39−44] All DFT calculations utilized the PBE0 functional. Geometry optimizations were carried out in Gaussian 16 rev. A.03, utilizing the def2-SVP basis set, while single point energy and TD-DFT calculations utilized the larger def2-TZVP basis set. CASSCF calculations were carried out to characterize the diradical character of the systems and utilized a minimal active space comprising four electrons distributed in four orbitals, [4,4], in combination with the def2-SVP basis set.[42] This active space has previously been validated to accurately describe the diradical character in TTFtt-bridged complexes.[28]

The predicted singlet (S_0 to S_1 and S_1 to S_0) transitions follow the same general trend as the experimental data; as the Hammett parameter decreases, the transitions are bathochromically shifted. The calculated natural transition orbitals (NTOs) also confirm that these transitions are largely TTFtt ligand-based $\pi-\pi$ transitions; however, we note slightly more Pt overlap as the Hammett parameter decreases, a sign of better energetic overlap and therefore increased delocalization (Figure 5). This behavior is somewhat counterintuitive, as increasing electron-withdrawing character with higher Hammett parameters might be expected to "pull" the orbital density further onto the Pt centers, thus leading to greater delocalization and a bathochromic shift. Instead, we see that increasing electron donation results in better energy matching between Pt and TTFtt and consequently increased delocalization. This improved energetic match is well captured through fragment analysis of the metal-capping ligand and TTFtt fragment energies (see Table S10).

Interestingly, the triplet absorptions do not shift as significantly as the singlet; however, the bathochromically shifted triplet values (relative to the predicted singlet absorptions) are consistent with the GSB shift we see after decay of the S_1 signal. This raises the possibility of independently tuning the singlet and triplet manifolds in these molecules.

The T_1-S_0 gap is also predicted to shift significantly across the series, from 3.83 kcal/mol for compound **5** to −0.09 kcal/mol for compound **4**. This changing gap trends linearly with J_{Pt-P}, indicating that this experimental value could be used as a predictive metric for the expected T_1-S_0 gap and thus as a tool to design systems with desired gap sizes. Furthermore, in addition to J_{Pt-P}, the T_1-S_0 gap also trends with the Hammett parameter, indicating that the donation of the para substituent (and the phosphine itself) is predicted to directly influence the ground state of the molecule (see Figures S105 and S106). Notably, the trend between T_1-S_0 gap and Hammett parameter is similar to the relationship between +1/+2 redox potential and Hammett parameter, again suggesting that even a slightly more donating para substituent may not only result in a far more reducing potential but also a well-separated triplet ground state.

Given that compound **4** is predicted to have a triplet ground state, we also performed calculations on the optimized triplet geometry in addition to the spin-unrestricted singlet geometry used for all of the other analogues. In the triplet geometry, the T_1-S_0 gap increases from −0.09 (singlet geometry) to 1.650 kcal/mol (triplet, see Table S10), suggesting that spin-unrestricted PBE0 poorly characterizes the open-shell singlet state of this complex. Because of this discrepancy, variable-temperature data is needed to confirm the ground state of the molecule.

Beyond the T_1-S_0 gap, diradical character is also predicted to increase as Hammett parameter decreases, from 0.881 in compound **1** to 1.130 in compound **4**. Notably, **4** in the triplet geometry has even higher diradical character, at 1.352 (see Table S10). We attribute this change in diradical character

https://doi.org/10.1021/jacs.4c04032
J. Am. Chem. Soc. 2024, 146, 17285−17295

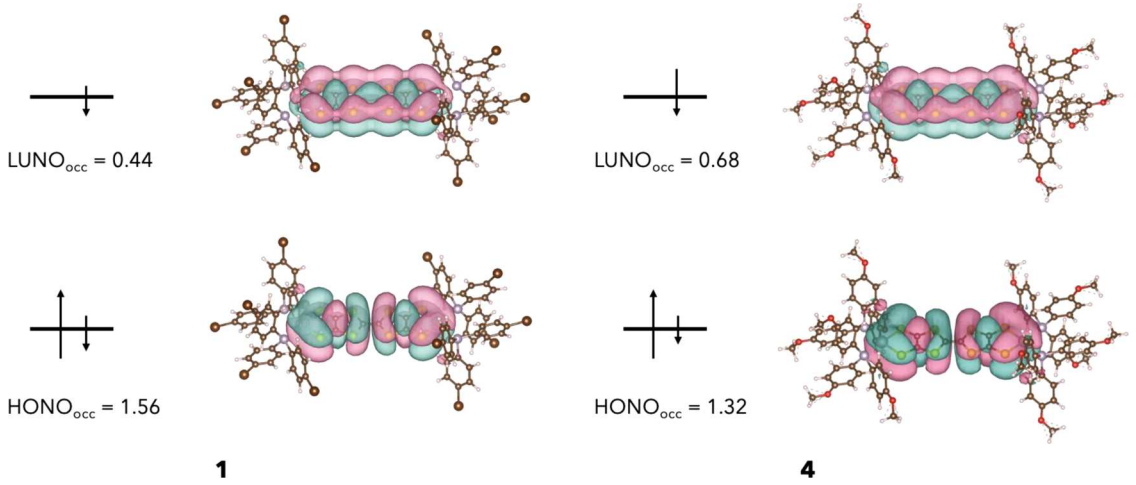

Figure 6. HONO-LUNO diagram of compounds **1** (left) and **4** (right), showing increased diradical character with para-substitution of more electron-donating groups on the triarylphosphine capping ligands.

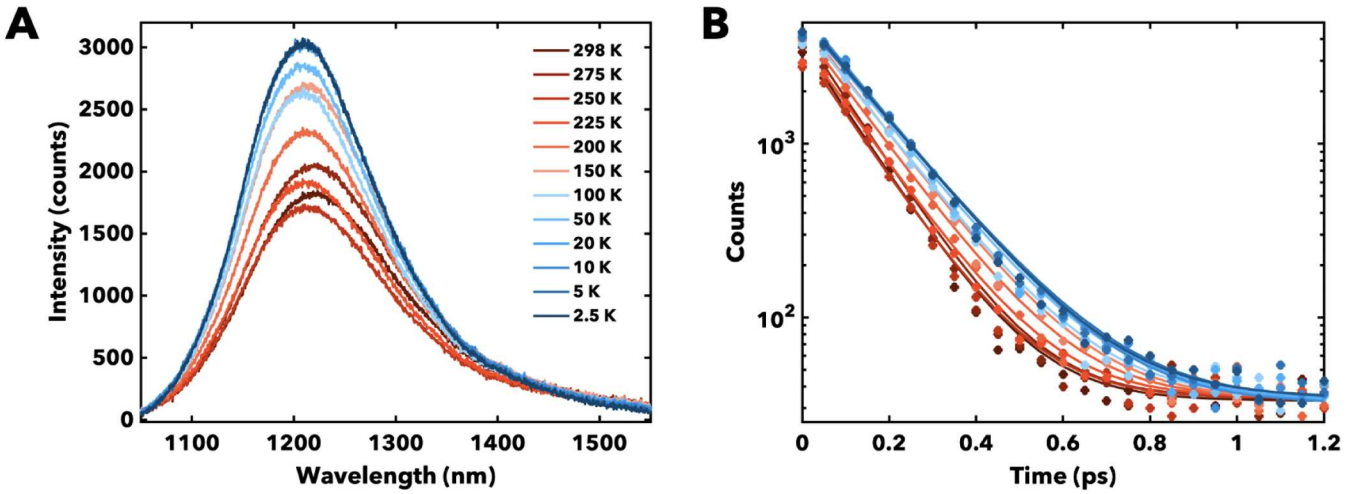

Figure 7. (A) Variable-temperature photoluminescence of compound **4** in polymer. (B) Variable-temperature TCSPC measurements of compound **4** in polymer.

across analogues to increased delocalization and a decreased T_1-S_0 gap (Figure 6).

Experimental Validation of Electronic Structure. We experimentally probed these predicted electronic structure changes via magnetic and photophysical measurements. Room-temperature Evans method measurements did not reveal major changes in triplet population across the series, although this data was acquired at elevated concentrations so it could be convoluted by aggregation; however, these measurements clearly confirm significant triplet population at room temperature across all analogues.

Variable-temperature photophysical measurements were carried out to determine the ground states for compounds **1**−**4** in polymer matrices to rule out any rigidification effects. No significant quenching of PL was seen upon cooling, and PL intensity continued to grow at low temperatures (see Figure 7A). Since luminescence arises from the singlet manifold, this increased PL intensity is indicative of a singlet ground state for compounds **1**−**4**.

Low-temperature TA also confirmed the population of S_1 for all four analogues, due to the continued presence of the characteristic GSB, ESA, and SE features down to 2.5 K. Lifetime saturation around 100 K was consistent with minimizing the ISC pathway seen in related systems (see Figure 7B).[20] A singlet ground state with a small T_1-S_0 gap is consistent with the predicted electronic structures for compounds **1**−**3**, **5**, and **6**; however, it is in contrast to the predicted triplet ground state for **4** in the optimized singlet geometry. Given the calculated small T_1-S_0 gap for compound **4** in either geometry, it is possible that the ground state might change given different conditions such as changing dielectrics or solid-state vs solution-phase measurements. It is also likely that a group more donating than OMe would stabilize the triplet ground state even further, opening up electronic structure design for TTFtt-based qubits.[45]

CONCLUSIONS

We synthesized a series of new Pt-capped TTFtt dicationic complexes and demonstrated facile tuning of their electronic structure via substitutions with commercially available triarylphosphines. Simple modification of the para substituent shifts absorption wavelengths >100 nm and emission wavelengths by ∼100 nm, allowing for optimization across common laser lines and communication bands. The solvatochromic behavior of this class of fluorophores also allows the absorption and emission range to be further expanded and distinguishes

https://doi.org/10.1021/jacs.4c04032
J. Am. Chem. Soc. 2024, 146, 17285−17295

these lumiphores as ratiometric imaging candidates. In addition to photophysical properties, the magnetic and electrochemical properties of the system can be significantly altered through the same para substituent, allowing for the design of optimized molecular imaging agents, sensors, and qubits. Lastly, this organic-based emission is retained in aqueous and acidic environments, demonstrating that this class of diradicaloid complexes are remarkably robust. This robustness, along with the facile manipulation and the sensitivity of these probes to their local environment, opens up the utility of these systems for applications such as multicolor imaging, NIR barcoding, and biological quantum sensing.

EXPERIMENTAL SECTION

General Synthetic Methods. All synthetic procedures were performed under inert conditions (dry N_2) in an MBraun UNIlab glovebox. Elemental analyses (C, H, N) were conducted by Midwest Microlabs. All solvents used were dried and purged with N_2 on a Pure Process Technology solvent system, and subsequently filtered through activated alumina and stored over 4 Å molecular sieves. TTFtt-$(SnBu_2)_2$,[27] $[Fc^{BzO}][BAr_4^F]$,[27] **5**,[19] **6**,[20] Pt{P(*p*-BrPh)$_3$}$_2$Cl$_2$,[23] Pt{P(*p*-FPh)$_3$}$_2$Cl$_2$,[24] Pt{P(*p*-CH_3Ph)$_3$}$_2$Cl$_2$,[25] and Pt{P(*p*-OCH_3Ph)$_3$}$_2$Cl$_2$[26] were prepared according to literature procedures. All other chemicals and reagents were purchased from commercial sources and used as received.

Synthesis and Characterization of 1. TTFtt$(SnBu_2)_2$ (0.043 g, 0.054 mmol) was dissolved in 4 mL of CH_2Cl_2 and slowly added to a solution of Pt{P(*p*-BrPh)$_3$}$_2$Cl$_2$ (0.137 g, 0.108 mmol) in 3 mL of CH_2Cl_2. The colorless solution formed a shiny salmon-brown suspension upon addition of the orange solution of TTFtt$(SnBu_2)_2$ and was left to stir for 10 min. Next, $[Fc^{BzO}][BAr_4^F]$ (0.130 g, 0.113 mmol) was dissolved in 4 mL of CH_2Cl_2 and slowly added to the stirring reaction. The salmon-brown suspension turned brown and then green upon full addition of $[Fc^{BzO}][BAr_4^F]$ and was subsequently left to stir for 5 min. The solution was condensed to 1 mL under vacuum, and petroleum ether (5 mL) was slowly added. Green crystals immediately began to form. The crystals were washed with petroleum ether several times (3 × 5 mL) and dried under vacuum. The crude product was redissolved in 2 mL of CH_2Cl_2, filtered through Celite, and layered with petroleum ether. The layered solution was cooled to −35 °C and left to crystallize overnight. The resulting green crystals were collected and dried (0.183 g, 77% yield). Crystals suitable for SXRD were selected from a CH_2Cl_2/petroleum ether slow diffusion gradient left to crystallize over a 2-day period at −35 °C. ^{1}H NMR (500 MHz, CD_2Cl_2, 298 K): δ 7.20−7.24 (24H, m, PPh_3), 7.50−7.52 (24H, m, PPh_3), 7.56 (8H, s, $[BAr_4^F]^-$), 7.73 (16H, s, $[BAr_4^F]^-$). ^{31}P{^{1}H} NMR (162 MHz, CD_2Cl_2, 298 K): δ 13.54 ($J_{Pt,P}$ = 3028 Hz). ^{195}Pt{^{1}H} NMR (107 MHz, CD_2Cl_2, 298 K): δ −4457.02 ($J_{Pt,P}$ = 3023 Hz). Anal. Calcd for **1**, $C_{142}H_{72}B_2F_{48}Pt_2P_4S_8Br_{12}$: C 38.40%, H 1.63%, N 0%; found: C 38.58%, H 1.65%, N none.

Synthesis and Characterization of 2. TTFtt$(SnBu_2)_2$ (0.030 g, 0.038 mmol) was dissolved in 4 mL of CH_2Cl_2 and slowly added to a solution of Pt{P(*p*-FPh)$_3$}$_2$Cl$_2$ (0.067 g, 0.075 mmol) in 3 mL of CH_2Cl_2. The colorless solution formed a shiny dark salmon suspension upon addition of the orange solution of TTFtt$(SnBu_2)_2$ and was left to stir for 10 min. Next, $[Fc^{BzO}][BAr_4^F]$ (0.090 g, 0.075 mmol) was dissolved in 4 mL of CH_2Cl_2 and slowly added to the stirring reaction. The dark salmon suspension turned dark brown and then green upon full addition of $[Fc^{BzO}][BAr_4^F]$ and was subsequently left to stir for 5 min. The solution was condensed to 1 mL under vacuum and petroleum ether (5 mL) was slowly added. Bright green crystals immediately began to form. The crystals were washed with petroleum ether several times (3 × 5 mL) and dried under vacuum. The crude product was redissolved in 2 mL of CH_2Cl_2, filtered through Celite, and layered with petroleum ether. The layered solution was cooled to −35 °C and left to crystallize overnight. The resulting green crystals were collected and dried (0.063 g, 45% yield). Crystals suitable for SXRD were selected from a CH_2Cl_2/petroleum ether slow diffusion gradient left to crystallize over a 2-day period at −35 °C. ^{1}H NMR (400 MHz, CD_2Cl_2, 298 K): δ 7.03−7.07 (24H, m, PPh_3), 7.35−7.41 (24H, m, PPh_3), 7.55 (8H, s, $[BAr_4^F]^-$), 7.73 (16H, s, $[BAr_4^F]^-$). ^{31}P{^{1}H} NMR (162 MHz, CD_2Cl_2, 298 K): δ 12.40 ($J_{Pt,P}$ = 3051 Hz). ^{195}Pt{^{1}H} NMR (107 MHz, CD_2Cl_2, 298 K): δ −4431.47 ($J_{Pt,P}$ = 3037 Hz). Anal. Calcd for **2**, $C_{142}H_{72}B_2F_{60}Pt_2P_4S_8$: C 45.97%, H 1.96%, N 0%; found: C 45.40%, H 1.95%, N none.

Synthesis and Characterization of 3. TTFtt$(SnBu_2)_2$ (0.015 g, 0.019 mmol) was dissolved in 3 mL of CH_2Cl_2 and slowly added to a solution of Pt{P(*p*-CH_3Ph)$_3$}$_2$Cl$_2$ (0.033 g, 0.038 mmol) in 3 mL of CH_2Cl_2. The colorless solution turned red upon addition of the orange solution of TTFtt$(SnBu_2)_2$ and was left to stir for 10 min. Next, $[Fc^{BzO}][BAr_4^F]$ (0.045 g, 0.039 mmol) was dissolved in 3 mL of CH_2Cl_2 and slowly added to the stirring reaction. The red solution turned dark brown and then green-brown upon full addition of $[Fc^{BzO}][BAr_4^F]$ and was subsequently left to stir for 5 min. The solution was condensed to 1 mL under vacuum and petroleum ether (5 mL) was slowly added. Green-brown solids began crashing out. The solids were washed with petroleum ether several times (3 × 5 mL) and dried under vacuum. The crude product was redissolved in 2 mL of CH_2Cl_2, filtered through Celite, and layered with petroleum ether. The layered solution was cooled to −35 °C and left to crystallize overnight. The resulting green-brown crystals were collected and dried (0.045 g, 65% yield). Crystals suitable for SXRD were selected from a CH_2Cl_2/petroleum ether slow diffusion gradient left to crystallize over a 2-day period at −35 °C. ^{1}H NMR (400 MHz, CD_2Cl_2, 298 K): δ 2.35 (36H, s, CH_3), 7.04−7.06 (24H, m, PPh_3), 7.23−7.28 (24H, m, PPh_3), 7.56 (8H, s, $[BAr_4^F]^-$), 7.73 (16H, s, $[BAr_4^F]^-$). ^{31}P{^{1}H} NMR (162 MHz, CD_2Cl_2, 298 K): δ 12.33 ($J_{Pt,P}$ = 3066 Hz). ^{195}Pt{^{1}H} NMR (107 MHz, CD_2Cl_2, 298 K): δ −4425.73 ($J_{Pt,P}$ = 3052 Hz). Anal. Calcd for **3**, $C_{154}H_{108}B_2F_{48}Pt_2P_4S_8$: C 50.50%, H 2.97%, N 0%; found: C 50.37%, H 2.72%, N none.

Synthesis and Characterization of 4. TTFtt$(SnBu_2)_2$ (0.032 g, 0.040 mmol) was dissolved in 4 mL of CH_2Cl_2 and oxidized with $[Fc^{BzO}][BAr_4^F]$ (0.093 g, 0.081 mmol) in 3 mL of CH_2Cl_2. The orange solution turned brown, then deep purple upon full addition of $[Fc^{BzO}][BAr_4^F]$ and was left to stir 5 min. A solution of Pt{P(*p*-OCH_3Ph)$_3$}$_2$Cl$_2$ (0.078 g, 0.080 mmol) in 3 mL of CH_2Cl_2 was slowly added. The purple solution turned green-brown upon addition of Pt{P(*p*-OCH_3Ph)$_3$}$_2$Cl$_2$ and was subsequently left to stir for 10 min. The solution was condensed to 1 mL under vacuum and petroleum ether (5 mL) was slowly added. Green-brown solids began crashing out. The solids were washed with petroleum ether several times (3 × 5 mL) and dried under vacuum. The crude product was redissolved in 2 mL of CH_2Cl_2, filtered through Celite, and layered with hexanes. The layered solution was cooled to −35 °C and left to crystallize overnight. The resulting green-brown crystals were collected and dried (0.066 g, 43% yield). Crystals suitable for SXRD were selected from a CH_2Cl_2/hexanes slow diffusion gradient left to crystallize over a 2-day period at −35 °C. ^{1}H NMR (400 MHz, CD_2Cl_2, 298 K): δ 3.80 (36H, s, OCH_3), 6.75−6.77 (24H, m, PPh_3), 7.27−7.32 (24H, m, PPh_3), 7.56 (8H, s, $[BAr_4^F]^-$), 7.72 (16H, s, $[BAr_4^F]^-$). ^{31}P{^{1}H} NMR (162 MHz, CD_2Cl_2, 298 K): δ 10.50 ($J_{Pt,P}$ = 3084 Hz). ^{195}Pt{^{1}H} NMR (107 MHz, CD_2Cl_2, 298 K): δ −4394.37 ($J_{Pt,P}$ = 3072 Hz). Anal. Calcd for **4**, $C_{154}H_{108}O_{12}B_2F_{48}Pt_2P_4S_8$: C 47.98%, H 2.82%, N 0%; found: C 48.13%, H 2.85%, N none.

CHARACTERIZATION AND ANALYSIS METHODS

Single-Crystal X-ray Diffraction (SXRD). All SXRD data were collected at 100 K on an XtalAB Synergy-S dual-source single-crystal X-ray diffractometer using a PhotonJet-S Cu (**1**, **2**, and **4**) or Mo (**3**) 50 W Microfocus X-ray source (λ = 1.5418 or 0.7107 Å, respectively) and a HyPix-6000HE Hybrid Photon Counting detector. Data reduction and integration were performed with the CryAlisPro 1.171.43.75a (Rigaku Oxford Diffraction, 2023) software package,

https://doi.org/10.1021/jacs.4c04032
J. Am. Chem. Soc. 2024, 146, 17285−17295

with numerical absorption correction based on Gaussian integration over a multifaceted crystal model and empirical absorption correction using spherical harmonics, implemented in the SCALE3 ABSPACK scaling algorithm. The structures were solved by SHELXT (version 2018/2)[46] and refined by a full-matrix least-squares procedure using OLEX2 (XL refinement program version 2018/3).[47,48] We note some A- and B-level alerts resulting from the propensity of the BAr_4^F counteranions to disorder and also from the commonly observed spurious electron density near the heavy metal, in these cases, Pt. In particular, the lack of rigidity in the methoxy groups of **4** potentially led to low crystallinity and loss of quality for this sample. We note that this was the best diffracting sample among numerous crystallization attempts.

Cyclic Voltammetry. Cyclic voltammetry measurements were performed using a glassy carbon working electrode, a silver wire pseudoreference, and a platinum wire counter electrode. Each voltammogram was referenced to an internal standard (Fc^+/Fc). All measurements were acquired using a BASi Epsilon potentiostat and analyzed using the BASi Epsilon software version 1.40.67NT.

Fourier Transform Infrared (FT-IR) Spectroscopy. All IR measurements were performed by drop-casting CH_2Cl_2 solutions onto KBr plates. Each spectrum was acquired on a Bruker Tensor II; both background subtractions and baseline corrections were applied for each complex using the OPUS software.

NMR Spectroscopy. ^1H, ^{31}P, and ^{195}Pt NMR spectra were acquired on Bruker DRX 400 and 500 spectrometers. Residual solvent peaks were referenced for all ^1H NMR measurements, and 85% phosphoric acid and sodium hexachloroplatinate were used as references for ^{31}P and ^{195}Pt NMR measurements, respectively. Evans method measurements were conducted in $CDCl_3$ with a capillary insert of 95/5% w/w $CDCl_3/CHCl_3$. Pascal's constants were used to correct for the diamagnetic contribution.[49]

UV−Vis−NIR. UV−vis−NIR measurements were performed using a Shimadzu UV-3600 Plus dual-beam spectrophotometer.

Photoluminescence Spectroscopy. Room-temperature emission spectra were acquired on a Horiba Fluorolog-3 spectrofluorometer equipped with a Synapse IGA-512X1-50-1700 InGaAs Array. Stability measurements were acquired on a Horiba Scientific PTI QuantaMaster fluorometer. Low-temperature emission spectra were recorded by loading samples in polymer onto a sapphire disk and cooling in a Janis cryostat.

Transient Absorption Spectroscopy. Transient absorption spectroscopy was performed using a 5 kHz amplified titanium:sapphire laser with a 120 fs laser pulse width. A portion of the 800 nm fundamental output was focused into a sapphire crystal to produce near-infrared continuum probe pulses that were mechanically delayed. Pump pulses were tuned to 950 nm using an optical parametric amplifier, and a mechanical chopper reduced the repetition rate to 2.5 kHz. Samples were excited with 0.2 mW of pump power.

Lifetime Measurements. Time-correlated single photon counting was performed on the samples using a 975 nm diode laser with a 60 ps pulse width operating at 20 MHz. Collected PL was dispersed using a 0.3 m spectrograph and detected with a superconducting nanowire single photon detector and multichannel scaler with 25 ps bin width. Of note, the instrument response function (IRF) falls around ∼60 ps.

Photoluminescence Quantum Yield Determination. The samples in 1 cm quartz fluorescence cuvettes (Starna) were normalized to optical densities at 900 nm using UV−vis−NIR measurements. All samples were kept at or below 0.1 OD at 900 nm to minimize reabsorption effects. Three different ODs were tested per sample, forming a gradient upon plotting against the integrated photoluminescence. The individual quantum yields were then calculated using this gradient and the reference method (reference is $[(dppePt)_2TTFtt][BAr^{F_4}]_2$, PLQY = 0.136% in DCM at 298 K[19]). The following equation was used

$$\mathrm{PLQY_s} = \mathrm{PLQY_r}\left(\frac{m_s}{m_r}\right)\left(\frac{n_s}{n_r}\right)^2$$

where m is the gradient of the OD vs integrated PL plot, n is the refractive index of the solvent, and r and s refer to the reference and the sample, respectively.

Radiative and Nonradiative Rate Determination. Both the experimentally determined quantum yield values, ϕ, and the TA singlet lifetimes were utilized to determine the nonradiative and radiative rate through the expression $\phi = k_r/(k_r + k_{nr})$, where the denominator, $(k_r + k_{nr})$, is the reciprocal of the TA lifetime, $\tau_{TA,S}$.

NIR Imaging Studies. The compounds were imaged using an Allied Vision Goldeye G-034 VSWIR TEC1 camera, mounted above a THORLABS 1000 nm long-pass filter (or an 1150 nm bandpass filter, dependent on the experiment). The samples rest on a stage below these two items and are orthogonally excited by an 808 nm fiber-coupled laser (THORLABS L808P200) operated at 250 mA.

Polymer Sample Preparation. The polymer samples for VT TCSPC, TA, and NIR barcoding experiments were prepared via dissolution of polymer (the polymer used throughout this study is poly(butyl methacrylate-*co*-isobutyl methacrylate)) and compound in dichloromethane and subsequent drop-casting onto either a microscope slide or sapphire disk. The optical density for all films was adjusted to 0.5 OD at the excitation wavelength.

■ ASSOCIATED CONTENT

Supporting Information

The Supporting Information is available free of charge at https://pubs.acs.org/doi/10.1021/jacs.4c04032.

Detailed experimental and computational procedures and additional spectra (PDF)

Accession Codes

CCDC 2341837−2341840 contain the supporting crystallographic data for this paper. These data can be obtained free of charge via www.ccdc.cam.ac.uk/data_request/cif, by emailing data_request@ccdc.cam.ac.uk, or by contacting The Cambridge Crystallographic Data Centre, 12 Union Road, Cambridge CB2 1EZ, U.K.; fax: +44 1223 336033.

■ AUTHOR INFORMATION

Corresponding Author

John S. Anderson − *Department of Chemistry, The University of Chicago, Chicago, Illinois 60637, United States;* orcid.org/0000-0002-0730-3018; Email: jsanderson@uchicago.edu

Authors

Lauren E. McNamara − *Department of Chemistry, The University of Chicago, Chicago, Illinois 60637, United States;* orcid.org/0000-0002-1169-8171

Jan-Niklas Boyn − *Department of Mechanical and Aerospace Engineering, Princeton University, Princeton, New Jersey 08544, United States;* orcid.org/0000-0002-6240-3759

Sophie W. Anferov − *Department of Chemistry, The University of Chicago, Chicago, Illinois 60637, United States;* orcid.org/0000-0003-3972-5845

Alexander S. Filatov − *Department of Chemistry, The University of Chicago, Chicago, Illinois 60637, United States;* orcid.org/0000-0002-8378-1994

Miles W. Maloney − *Department of Chemistry, The University of Chicago, Chicago, Illinois 60637, United States*

David A. Mazziotti − *Department of Chemistry, The University of Chicago, Chicago, Illinois 60637, United States;* orcid.org/0000-0002-9938-3886

Richard D. Schaller − *Center for Nanoscale Materials, Argonne National Laboratory, Argonne, Illinois 60439, United States; Department of Chemistry, Northwestern*

University, Evanston, Illinois 60208, United States;
orcid.org/0000-0001-9696-8830

Complete contact information is available at:
https://pubs.acs.org/10.1021/jacs.4c04032

Notes

The authors declare the following competing financial interest(s): L.E.M., J.S.A, and R.D.S. have a patent filed on a portion of this work.

■ ACKNOWLEDGMENTS

J.S.A. and D.A.M. gratefully acknowledge support for this work from the U.S. Department of Energy, Office of Science, Office of Basic Energy Sciences, under Grant DE-SC0019215. J.S.A. also gratefully acknowledges support from the 3M corporation through an NTFA and the Army Research Office under Grant W911NF-20-1-0091. This work was supported by the Chicago MRSEC, which is funded by NSF through Grant DMR-1420709. D.A.M. also gratefully acknowledges support from the ACS Petroleum Research Fund Grant No. PRF No. 61644-ND6 and the U.S. National Science Foundation Grant No. CHE-2155082. This work was performed, in part, at the Center for Nanoscale Materials, a DOE Office of Science User Facility, and supported by the U.S. Department of Energy, Office of Science, Office of Basic Energy Sciences under Contract No. DE-AC02-06CH11357. Parts of this work were performed at the Soft Matter Characterization Facility at the Pritzker School of Molecular Engineering at the University of Chicago. This work made use of the IMSERC Crystallography facility at Northwestern University, which has received support from the Soft and Hybrid Nanotechnology Experimental (SHyNE) Resource (NSF ECCS-2025633), Northwestern University. The authors also thank Charlotte Stern and Christos D. Malliakas for their assistance with SXRD acquisition at IMSERC. They also gratefully acknowledge Graftek Imaging, Inc. and Robert Eastlund for the use of the Allied Vision VSWIR camera. Ningxin Jiang and Joe Scott are thanked for helpful discussions.

■ REFERENCES

(1) Hong, G.; Antaris, A. L.; Dai, H. Near-Infrared Fluorophores for Biomedical Imaging. *Nat. Biomed. Eng.* **2017**, *1* (1), No. 0010.
(2) Matsui, A.; Tanaka, E.; Choi, H. S.; Winer, J. H.; Kianzad, V.; Gioux, S.; Laurence, R. G.; Frangioni, J. V. Real-Time Intra-Operative near-Infrared Fluorescence Identification of the Extrahepatic Bile Ducts Using Clinically Available Contrast Agents. *Surgery* **2010**, *148* (1), 87−95.
(3) Li, B.; Zhao, M.; Feng, L.; Dou, C.; Ding, S.; Zhou, G.; Lu, L.; Zhang, H.; Chen, F.; Li, X.; Li, G.; Zhao, S.; Jiang, C.; Wang, Y.; Zhao, D.; Cheng, Y.; Zhang, F. Organic NIR-II Molecule with Long Blood Half-Life for in Vivo Dynamic Vascular Imaging. *Nat. Commun.* **2020**, *11* (1), No. 3102.
(4) Qu, C.; Xiao, Y.; Zhou, H.; Ding, B.; Li, A.; Lin, J.; Zeng, X.; Chen, H.; Qian, K.; Zhang, X.; Fang, W.; Wu, J.; Deng, Z.; Cheng, Z.; Hong, X. Quaternary Ammonium Salt Based NIR-II Probes for In Vivo Imaging. *Adv. Opt. Mater.* **2019**, *7* (15), No. 1900229.
(5) Zeng, X.; Xiao, Y.; Lin, J.; Li, S.; Zhou, H.; Nong, J.; Xu, G.; Wang, H.; Xu, F.; Wu, J.; Deng, Z.; Hong, X. Near-Infrared II Dye-Protein Complex for Biomedical Imaging and Imaging-Guided Photothermal Therapy. *Adv. Healthcare Mater.* **2018**, *7* (18), No. 1800589.
(6) Antaris, A. L.; Chen, H.; Diao, S.; Ma, Z.; Zhang, Z.; Zhu, S.; Wang, J.; Lozano, A. X.; Fan, Q.; Chew, L.; Zhu, M.; Cheng, K.; Hong, X.; Dai, H.; Cheng, Z. A High Quantum Yield Molecule-Protein Complex Fluorophore for near-Infrared II Imaging. *Nat. Commun.* **2017**, *8* (1), No. 15269.
(7) Wu, J.-J.; Wang, X.-D.; Liao, L.-S. Near-Infrared Solid-State Lasers Based on Small Organic Molecules. *ACS Photonics* **2019**, *6* (11), 2590−2599.
(8) Song, Y.; Yu, G.; Xie, B.; Zhang, K.; Huang, F. Visible-to-near-Infrared Organic Photodiodes with Performance Comparable to Commercial Silicon-Based Detectors. *Appl. Phys. Lett.* **2020**, *117* (9), No. 093302.
(9) Ho, C.-L.; Li, H.; Wong, W.-Y. Red to Near-Infrared Organometallic Phosphorescent Dyes for OLED Applications. *J. Organomet. Chem.* **2014**, *751*, 261−285.
(10) Liu, S.; Xu, W.; Li, X.; Pang, D.-W.; Xiong, H. BOIMPY-Based NIR-II Fluorophore with High Brightness and Long Absorption beyond 1000 Nm for In Vivo Bioimaging: Synergistic Steric Regulation Strategy. *ACS Nano* **2022**, *16* (10), 17424−17434.
(11) Wan, H.; Yue, J.; Zhu, S.; Uno, T.; Zhang, X.; Yang, Q.; Yu, K.; Hong, G.; Wang, J.; Li, L.; Ma, Z.; Gao, H.; Zhong, Y.; Su, J.; Antaris, A. L.; Xia, Y.; Luo, J.; Liang, Y.; Dai, H. A Bright Organic NIR-II Nanofluorophore for Three-Dimensional Imaging into Biological Tissues. *Nat. Commun.* **2018**, *9* (1), No. 1171.
(12) Ashoka, A. H.; Ashokkumar, P.; Kovtun, Y. P.; Klymchenko, A. S. Solvatochromic Near-Infrared Probe for Polarity Mapping of Biomembranes and Lipid Droplets in Cells under Stress. *J. Phys. Chem. Lett.* **2019**, *10* (10), 2414−2421.
(13) Collot, M.; Fam, T. K.; Ashokkumar, P.; Faklaris, O.; Galli, T.; Danglot, L.; Klymchenko, A. S. Ultrabright and Fluorogenic Probes for Multicolor Imaging and Tracking of Lipid Droplets in Cells and Tissues. *J. Am. Chem. Soc.* **2018**, *140* (16), 5401−5411.
(14) Berezin, M. Y.; Lee, H.; Akers, W.; Achilefu, S. Near Infrared Dyes as Lifetime Solvatochromic Probes for Micropolarity Measurements of Biological Systems. *Biophys. J.* **2007**, *93* (8), 2892−2899.
(15) Wang, S.; Fan, Y.; Li, D.; Sun, C.; Lei, Z.; Lu, L.; Wang, T.; Zhang, F. Anti-Quenching NIR-II Molecular Fluorophores for in Vivo High-Contrast Imaging and pH Sensing. *Nat. Commun.* **2019**, *10* (1), No. 1058.
(16) Zhou, Z.; Yang, K.; He, L.; Wang, W.; Lai, W.; Yang, Y.; Dong, Y.; Xie, S.; Yuan, L.; Zeng, Z. Sulfone-Functionalized Chichibabin's Hydrocarbons: Stable Diradicaloids with Symmetry Breaking Charge Transfer Contributing to NIR Emission beyond 900 Nm. *J. Am. Chem. Soc.* **2024**, *146* (10), 6763−6772.
(17) Borel, A.; Habrant-Claude, T.; Rapisarda, F.; Reichel, J.; Doorn, S. K.; Voisin, C.; Chassagneux, Y. Telecom Band Single-Photon Source Using a Grafted Carbon Nanotube Coupled to a Fiber Fabry−Perot Cavity in the Purcell Regime. *ACS Photonics* **2023**, *10* (8), 2839−2845.
(18) Adewuyi, J. A.; Ung, G. High Quantum Yields from Perfluorinated Binolate Erbium Complexes and Their Circularly Polarized Luminescence. *J. Am. Chem. Soc.* **2024**, *146* (10), 7097−7104.
(19) McNamara, L. E.; Boyn, J.-N.; Melnychuk, C.; Anferov, S. W.; Mazziotti, D. A.; Schaller, R. D.; Anderson, J. S. Bright, Modular, and Switchable Near-Infrared II Emission from Compact Tetrathiafulvalene-Based Diradicaloid Complexes. *J. Am. Chem. Soc.* **2022**, *144* (36), 16447−16455.
(20) McNamara, L. E.; Melnychuk, C.; Boyn, J.-N.; Anferov, S. W.; Mazziotti, D. A.; Schaller, R. D.; Anderson, J. S. Elucidating Non-Radiative Decay in near-Infrared Lumiphores: Leveraging New Design Principles to Develop a Telecom Band Organic Dye Laser. *Chem* **2024**, 1−17, DOI: 10.1016/j.chempr.2024.03.023.
(21) Dado, R. S.; McNamara, L. E.; Powers-Nash, M.; Anderson, J. S. Heteroatom Substitution for the Development of Near-IR Lumiphores. *Trends Chem.* **2023**, *5* (8), 581−583.
(22) Hansch, C.; Leo, A.; Taft, R. W. A Survey of Hammett Substituent Constants and Resonance and Field Parameters. *Chem. Rev.* **1991**, *91* (2), 165−195.
(23) Louch, W. J.; Eaton, D. R. The 19F Chemical Shifts of Fluorophenyl Phosphine Complexes of Group VIII Metals. *Inorg. Chim. Acta* **1978**, *30*, 215−220.

(24) Adams, D. J.; Bennett, J. A.; Duncan, D.; Hope, E. G.; Hopewell, J.; Stuart, A. M.; West, A. J. Synthesis and Characterisation of Trisarylphosphine Selenides: Further Insight into the Effect of Fluoroalkylation on the Electronic Properties of Trisarylphosphines. *Polyhedron* **2007**, *26* (7), 1505−1513.
(25) Al-Najjar, I. M. 31P and 195Pt NMR Characteristics of New Binuclear Complexes of [Pt2 × 4](PR3)2] *Cis/Trans* Isomers and of Mononuclear Analogs. *Inorg. Chim. Acta* **1987**, *128* (1), 93−104.
(26) Decker, C.; Henderson, W.; Nicholson, B. K. Triphenyl-Phosphine and -Arsine Analogues Which Facilitate the Electrospray Mass Spectrometric Analysis of Neutral Metal Complexes. *J. Chem. Soc., Dalton Trans.* **1999**, No. 19, 3507−3513.
(27) Xie, J.; Boyn, J.-N.; Filatov, A. S.; McNeece, A. J.; Mazziotti, D. A.; Anderson, J. S. Redox, Transmetalation, and Stacking Properties of Tetrathiafulvalene-2,3,6,7-Tetrathiolate Bridged Tin, Nickel, and Palladium Compounds. *Chem. Sci.* **2020**, *11* (4), 1066−1078.
(28) Boyn, J.-N.; McNamara, L. E.; Anderson, J. S.; Mazziotti, D. A. Interplay of Electronic and Geometric Structure Tunes Organic Biradical Character in Bimetallic Tetrathiafulvalene Tetrathiolate Complexes. *J. Phys. Chem. A* **2022**, *126* (21), 3329−3337.
(29) Lee, G.; Mun, J.; Choi, H.; Han, S.; Kwang Hahn, S. Multispectral Upconversion Nanoparticles for near Infrared Encoding of Wearable Devices. *RSC Adv.* **2021**, *11* (36), 21897−21903.
(30) Leng, Y.; Wu, W.; Li, L.; Lin, K.; Sun, K.; Chen, X.; Li, W. Magnetic/Fluorescent Barcodes Based on Cadmium-Free Near-Infrared-Emitting Quantum Dots for Multiplexed Detection. *Adv. Funct. Mater.* **2016**, *26* (42), 7581−7589.
(31) Baride, A.; Meruga, J. M.; Douma, C.; Langerman, D.; Crawford, G.; Kellar, J. J.; Cross, W. M.; May, P. S. A NIR-to-NIR Upconversion Luminescence System for Security Printing Applications. *RSC Adv.* **2015**, *5* (123), 101338−101346.
(32) White, K. A.; Chengelis, D. A.; Gogick, K. A.; Stehman, J.; Rosi, N. L.; Petoud, S. Near-Infrared Luminescent Lanthanide MOF Barcodes. *J. Am. Chem. Soc.* **2009**, *131* (50), 18069−18071.
(33) Englman, R.; Jortner, J. The Energy Gap Law for Radiationless Transitions in Large Molecules. *Mol. Phys.* **1970**, *18* (2), 145−164.
(34) Friedman, H. C.; Cosco, E. D.; Atallah, T. L.; Jia, S.; Sletten, E. M.; Caram, J. R. Establishing Design Principles for Emissive Organic SWIR Chromophores from Energy Gap Laws. *Chem* **2021**, *7* (12), 3359−3376.
(35) Lin, S. H. Energy Gap Law and Franck−Condon Factor in Radiationless Transitions. *J. Chem. Phys.* **1970**, *53* (9), 3766−3767.
(36) Yang, Q.; Ma, H.; Liang, Y.; Dai, H. Rational Design of High Brightness NIR-II Organic Dyes with S-D-A-D-S Structure. *Acc. Mater. Res.* **2021**, *2* (3), 170−183.
(37) Zhao, X.; Cheng, J.; Zhang, L.; Yun, B.; Yan, K.; Wu, B.; Liu, X.; Zhang, F.; Lei, Z. Near-Infrared II Emissive Diphenylaminoacridine Based on the Planarized Intramolecular Charge Transfer Mechanism. *Cell Rep. Phys. Sci.* **2023**, *4* (12), No. 101691.
(38) Mi, C.; Guan, M.; Zhang, X.; Yang, L.; Wu, S.; Yang, Z.; Guo, Z.; Liao, J.; Zhou, J.; Lin, F.; Ma, E.; Jin, D.; Yuan, X. High Spatial and Temporal Resolution NIR-IIb Gastrointestinal Imaging in Mice. *Nano Lett.* **2022**, *22* (7), 2793−2800.
(39) Adamo, C.; Barone, V. Toward Reliable Density Functional Methods without Adjustable Parameters: The PBE0Model. *J. Chem. Phys.* **1999**, *110* (13), 6158−6170.
(40) Weigend, F.; Ahlrichs, R. Balanced Basis Sets of Split Valence, Triple Zeta Valence and Quadruple Zeta Valence Quality for H to Rn: Design and Assessment of Accuracy. *Phys. Chem. Chem. Phys.* **2005**, *7* (18), 3297−3305.
(41) Frisch, M. J.; Trucks, G. W.; Schlegel, H. B.; Scuseria, G. E.; Robb, M. A.; Cheeseman, J. R.; Scalmani, G.; Barone, V.; Petersson, G. A.; Nakatsuji, H.; Li, X.; Caricato, M.; Marenich, A. V.; Bloino, J.; Janesko, R.; Gomperts, R.; Mennucci, B.; Hratchian, H. P.; Ortiz, J. V.; Izmaylov, A. F.; Sonnenberg, J. L.; Williams-Young, D.; Ding, F.; Lipparini, F.; Egidi, F.; Goings, J.; Peng, A.; Petrone, A.; Henderson, T.; Ranasinghe, D.; Zakrzewski, V. G.; Gao, J.; Rega, N.; Zheng, G.; Liang, W.; Hada, M.; Ehara, M.; Toyota, K.; Fukuda, R.; Hasegawa, J.; Ishida, M.; Nakajima, T.; Honda, Y.; Kitao, O.; Nakai, H.; Vreven, T.; Throssell, K.; Montgomery, J. A.; Peralta, J. E.; Ogliaro, F.; Bearpark, M.; Heyd, J. J.; Brothers, E.; Kudin, K. N.; Staroverov, V. N.; Keith, T. A.; Kobayashi, R.; Normand, J.; Raghavachari, K.; Rendell, A.; Burant, J. C.; Iyengar, S. S.; Tomasi, J.; Cossi, M.; Millam, J. M.; Klene, M.; Adamo, C.; Cammi, R.; Ochterski, J. W.; Martin, R. L.; Morokuma, K.; Farkas, O.; Foresman, J. B.; Fox, D. J. *Gaussian 16*, Revision C.01; Gaussian, Inc., 2016.
(42) Neese, F.; Wennmohs, F.; Becker, U.; Riplinger, C. The ORCA Quantum Chemistry Program Package. *J. Chem. Phys.* **2020**, *152* (22), No. 224108.
(43) Neese, F.; Wennmohs, F.; Hansen, A.; Becker, U. Efficient, Approximate and Parallel Hartree−Fock and Hybrid DFT Calculations. A 'Chain-of-Spheres' Algorithm for the Hartree−Fock Exchange. *Chem. Phys.* **2009**, *356* (1), 98−109.
(44) Weigend, F. Accurate Coulomb-Fitting Basis Sets for H to Rn. *Phys. Chem. Chem. Phys.* **2006**, *8* (9), 1057−1065.
(45) McNamara, L. E.; Zhou, A.; Rajh, T.; Sun, L.; Anderson, J. S. Realizing Solution-Phase Room Temperature Quantum Coherence in a Tetrathiafulvalene-Based Diradicaloid Complex. *Cell Rep. Phys. Sci.* **2023**, *4* (12), No. 101693.
(46) Sheldrick, G. M. SHELXT − Integrated Space-Group and Crystal-Structure Determination. *Acta Crystallogr., Sect. A: Found. Adv.* **2015**, *71* (1), 3−8.
(47) Sheldrick, G. M. Crystal Structure Refinement with SHELXL. *Acta Crystallogr., Sect. C: Struct. Chem.* **2015**, *71* (1), 3−8.
(48) Dolomanov, O. V.; Bourhis, L. J.; Gildea, R. J.; Howard, J. A. K.; Puschmann, H. OLEX2: A Complete Structure Solution, Refinement and Analysis Program. *J. Appl. Crystallogr.* **2009**, *42* (2), 339−341.
(49) Bain, G. A.; Berry, J. F. Diamagnetic Corrections and Pascal's Constants. *J. Chem. Educ.* **2008**, *85* (4), 532.

https://doi.org/10.1021/jacs.4c04032
J. Am. Chem. Soc. 2024, 146, 17285−17295